Journal of Advanced Ceramics
2023, **12**(5): 1001–1014
https://doi.org/10.26599/JAC.2023.9220734
ISSN 2226-4108
CN 10-1154/TQ

Research Article

Abnormal thermal expansion coefficients in $(Nd_{1-x}Dy_x)_2Zr_2O_7$ pyrochlore: The effect of low-lying optical phonons

Zesheng Yang[a,†], Yi Li[a,b,†], Wei Pan[a], Chunlei Wan[a,*]

[a]*State Key Laboratory of New Ceramics & Fine Processing*, *Tsinghua University*, *Beijing 100084*, *China*
[b]*College of Mathematics and Physics*, *Beijing University of Chemical Technology*, *Beijing 100029*, *China*

Received: December 12, 2022; Revised: January 24, 2023; Accepted: February 20, 2023

Abstract: Chemical doping is a normal strategy to tune thermal expansion coefficient (TEC) of ceramics in engineering applications, but the resultant TEC values usually follow Vegard's law, as doping does not modify the nature of chemical bonding in ceramics and its anharmonicity. In this paper, we report abnormal TEC behavior in $(Nd_{1-x}Dy_x)_2Zr_2O_7$ ceramics, where the TEC values remarkably exceed the values predicted by Vegard's law and even exceed the values obtained for two constituents $Nd_2Zr_2O_7$ and $Dy_2Zr_2O_7$. In addition to a reduction in lattice energy with an increasing molar fraction of Dy (x) value, we attribute the additional increase in the TEC to the high concentration of Dy dopants in a pyrochlore (P) region, which can soften low-lying optical phonon modes and induce strongly avoided crossing with acoustic phonon branches and enhanced anharmonicity. We believe that this finding can provide a new route to break through the restriction imposed by the conventional Vegard's law on the TEC values and bring new opportunities for thermal barrier coatings (TBCs) or ceramic/metal composites towards realizing minimized thermal mismatch and prolonged service life during thermal cycling.

Keywords: thermal barrier coating (TBC); thermal expansion; first-principles calculations; avoided crossing

1 Introduction

Thermal expansion properties are crucial in engineering materials that operate over a wide range of temperatures. In particular, in composites or coating systems with heterointerfaces, the thermal expansion mismatch between different materials can become a major concern regarding durability of a system in service during thermal cycling. Ceramics and metals, which have different thermal expansion coefficients (TECs), are always integrated together in the form of composites or coatings [1–3]. Considering the relatively low thermal expansion properties of ceramic materials, it is necessary to increase the TEC of the ceramic materials to match that of the metals, which can effectively alleviate internal thermal strain with prolonged service life.

Thermal barrier coatings (TBCs) have been widely used to protect hot-section metallic parts in gas-turbine engines [4]. Typical TBC systems contain metallic bond coats and ceramic top coats. The metallic bond coat with a typical composition MCrAlY (M = Ni or Co) protects an alloy substrate from corrosion and

† Zesheng Yang and Yi Li contributed equally to this work.
* Corresponding author.
E-mail: wancl@mail.tsinghua.edu.cn

enhances the bonding between the substrate and the top coat. The top coat requires low thermal conductivity (κ) to provide a temperature gradient across the coating [5]. During the operation, the TBC system undergoes a harsh thermal cycling process, and the thermal expansion mismatch between the bond coat and the top coat is fatal for durability of the TBCs. The TEC of the typical NiCoCrAlY bond coat is 17.5×10^{-6} K^{-1}, while the ceramic top coat possesses a much lower TEC of approximately 10×10^{-6} K^{-1} [6]. In this case, thermal stress in the bond coat is proportional to the thermal expansion difference between the bond coat and the top coat, and hoop compression occurs in the top coat [7]. When the thermal stress exceeds the fracture critical point, cracks occur in the top coat, which is one of the most important failure mechanisms in the TBC systems. For further improvements in the durability of gas-turbine engines, the TEC of the top coat ceramics should be enhanced to approach the value of the bond coat.

In recent years, rare-earth zirconates ($RE_2Zr_2O_7$) have been identified as the next-generation top coat materials with better phase stability, lower thermal conductivity, and better calcium–magnesium–aluminum–silicate (CMAS) corrosion resistance than the previously used 8 wt% yttria-stabilized zirconia (8YSZ) [8–10]. The TEC of $RE_2Zr_2O_7$ is approximately $(9.6–11.0)\times10^{-6}$ K^{-1} [11]. The thermal expansion properties are directly affected by the lattice energy, which can be altered through doping. $RE_2Zr_2O_7$ belongs to a large complex oxide group with the general formula $A_2B_2O_7$, and their structures depend on a cation radius ratio of A and B (r_A/r_B) [12]. Because of the different chemical environments at the A site and B site and diverse ionic sizes, masses, and valences, several doping mechanisms in $RE_2Zr_2O_7$ show different influences on the thermal expansion properties. A-site substitutional doping has been widely researched because of the variety of lanthanide elements which have similar chemical properties. Lehmann *et al*. [13] substituted 30 mol% Nd, Eu, and Gd and 15 mol% Dy into the lattice of $La_2Zr_2O_7$, together with three other 100 mol% substitution compositions, $Nd_2Zr_2O_7$, $Eu_2Zr_2O_7$, and $Gd_2Zr_2O_7$. Though the TECs of partial substitution compositions are improved, they are still lower than the 100 mol% substitution compositions. In other words, the TECs of binary compositions ranged between both pure components. The underlying reason is that the substitution does not modify the nature of chemical bonds and anharmonicity, which is essential for the TEC. We will use Vegard's law, which conventionally indicates the linear relationship between the crystal lattice constant of a binary mixture and the concentration of constituent components, to describe similar characteristics of the TEC values in binary systems. In other substitutional lanthanide zirconate systems, such as $(La_{1-x}Yb_x)_2Zr_2O_7$, $(Nd_{1-x}Gd_x)_2Zr_2O_7$, and $(Yb_xGd_{1-x})_2Zr_2O_7$ [14–16], the TEC values of solid solution are also not higher than those of either end component but nearly follow Vegard's law. The TEC variation after B-site substitutional doping was also investigated. In $Yb_2(Zr_{1-x}Ce_x)_2O_7$, Ce^{4+} with a larger radius leads to a higher lattice parameter and more distortion, then binding energy is reduced, and the TEC values increase with the increasing Ce content [17]. However, the partial reduction of Ce^{4+} to Ce^{3+} happens at elevated temperatures, which brings risks during service. Ti^{4+} with a smaller radius than Zr^{4+} has also been substituted into the B site, and the TEC values of $Gd_2(Zr_{1-x}Ti_x)_2O_7$ reach a maximum at $x = 0.2$ (In Ref. [18], x is the molar fraction of Ti). Initial Ti^{4+} substitution results in the perturbation of corner-sharing BO_6 octahedra, which maintains structural integrity of pyrochlore (P). As a result, the TEC is enhanced at first. However, increasing the Ti^{4+} content in the B site causes larger r_A/r_B, and then drives long-range ordering which enhances the Madelung constant (A) of pyrochlore. Meanwhile, smaller Ti^{4+} leads to unit cell contraction, so higher lattice energy results in a lower TEC [18]. In substitutional solid solution, though non-Vegard behavior appears in some systems, the TEC improvement degree is relatively low. Compared with the substitutional doping, interstitial doping in pyrochlore is better for achieving the non-Vegard behavior of the TEC in $RE_2Zr_2O_7$. The cations with much smaller sizes are doped into the lattice in the form of oxides, such as Mg^{2+} and Sc^{3+} [19–21]. First, the interstitial ions expand the lattice. Secondly, the interstitial O^{2-} anion takes the site of 8*a* vacancy, which increases the free parameter (ε) of the crystal structure of 48*f* oxygen because of repulsion. In a pyrochlore structure, the ε-parameter plays an important role; it determines shapes of AO_8 and BO_6 polyhedra, and Madelung energy decreases with the increasing ε. Consequently, the TEC values increase when the doping amount is low. When smaller cations enter the

lattice, they will substitute RE^{3+} or form a second phase with a lower TEC, and then the TEC values reduce. However, the radii of these dopants are quite different from those of lanthanide RE elements, and the risk of inhomogeneous composition could exist in high-temperature applications. In summary, the attempts towards enhanced thermal expansion properties for $RE_2Zr_2O_7$ have been focused on changing the lattice energy and key structure parameter of pyrochlore, but there is still a lack of materials with the highly improved TEC and good thermal stability.

In this paper, we propose a new route to improve the thermal expansion properties in a binary $RE_2Zr_2O_7$ system $(Nd_{1-x}Dy_x)_2Zr_2O_7$ that can go beyond Vegard's law. Through the careful design of the ratio of the radii between the A and B sites, $(Nd_{1-x}Dy_x)_2Zr_2O_7$ can maintain the pyrochlore structure within a wide composition range. In addition to a reduction in the lattice energy, the high concentration of heavy Dy dopants in pyrochlore solid solution softens the low-lying optical phonon modes. These optical branches mix with the acoustic phonon branches and form the separated phonon bands that contain both optical part and acoustic part. This phenomenon is known as "avoided crossing" [22], which leads to enhanced anharmonicity. Thus, the TEC values of $(Nd_{1-x}Dy_x)_2Zr_2O_7$ are much higher than the values predicted by Vegard's law in the whole pyrochlore region. In particular, for a wide composition range of $0.3 < x < 0.6$, $(Nd_{1-x}Dy_x)_2Zr_2O_7$ shows higher TEC values than the pure components $Nd_2Zr_2O_7$ and $Dy_2Zr_2O_7$. The dopants and hosts have similar properties because they are both the lanthanide elements, leading to better thermal stability than interstitial ion doping. We believe that this finding can provide new opportunities in the TBC systems towards minimizing the thermal mismatch between the ceramic coating and the metallic substrate and improving the corresponding thermal stability.

2 Experimental and calculation methods

2. 1 Experimental details

$(Nd_{1-x}Dy_x)_2Zr_2O_7$ (x = 0, 0.1, 0.2, 0.3, 0.4, 0.5, 0.6, 0.7, 0.8, 0.9, and 1) ceramic powders were synthesized by the solid reaction method. Raw oxides (Nd_2O_3, Dy_2O_3, and ZrO_2) were calcined at 1000 ℃ for 5 h to remove absorbed water and carbon dioxide, and then weighed according to the stoichiometric ratio. The weighed starting materials were mixed and ball-milled with ethanol at 250 r/min for 5 h, and then slurries were rotationally evaporated, dried, and precalcined at 1250 ℃ for 5 h. The calcined powders were ground and ball-milled again at 250 r/min for 10 h. After drying, the newly obtained powders were sieved through a 200-mesh screen and pressed to form green bodies. Finally, the green bodies were isostatically cold pressed at 200 MPa, and then calcined pressureless in air at 1600 ℃ for 10 h to obtain dense ceramic samples.

Phase structures of the samples were characterized by an X-ray diffractometer (D/max-RB, Rigaku, Japan) with Cu Kα radiation by 8° min^{-1} continuous scanning from 2θ = 10° to 90°. Rietveld refinement was carried out using the Fullprof software [23], and data were obtained by continuous scanning at 2° min^{-1} from 2θ = 10° to 120°. Appropriate structural models and scale parameters were used at the beginning, backgrounds were fitted with a sixth-order polynomial function, and peaks were fitted with a pseudo-Voigt profile function. A Raman spectrometer (532 nm; LabRAM HR800, Horiba, Japan) was also utilized because of its sensitivity to detect order–disorder transitions. The wavenumber range was 100–1000 cm^{-1}, and the signal was accumulated by 10 scans.

The TECs of the samples were measured through a thermomechanical analyzer (TMA402F3, NETZSCH, Germany) up to 1400 ℃. Before measurement, the samples were machined to dimensions of 25 mm × 3 mm × 3 mm; a baseline using a standard Al_2O_3 sample was first obtained to eliminate the effect of sample holders. The TEC value was calculated by Eq. (1):

$$\mathrm{TEC} = \frac{L - L_0}{L_0(T - T_0)} \tag{1}$$

where T_0 (= 40 ℃ in this article) is the reference temperature, and L_0 is the length of the sample at T_0. L is the length of the sample at the temperature (T).

The thermal diffusivities (D) for the samples of x = 0 and x = 0.5 were measured by a laser flash analyzer (LFA467, NETZSCH, Germany) in an argon atmosphere. Before measurement, the samples were machined into plates with dimensions of ϕ10 mm × 1 mm, and a thin layer of Pt was deposited onto the sample surface. The κ was calculated by Eq. (2):

$$\kappa = D c_p \rho \tag{2}$$

The heat capacity (c_p) was calculated by Neumann–

Kopp law based on the values of the constituent oxides obtained from Ref. [24]. The density (ρ) was measured by Archimedes method. The theoretical density was calculated using X-ray diffraction (XRD) refinement results, and then the porosity (φ) was obtained. We obtained almost fully dense ceramic for all the samples, and their φ were lower than 5%. Considering the effect of φ on the thermal conductivity, the thermal conductivity (κ_0) of the dense material was corrected as

$$\kappa_0 = \kappa/(1-1.5\varphi) \quad (3)$$

2.2 Calculation details

Lattice structures of $Nd_2Zr_2O_7$ (pyrochlore phase) and $Dy_2Zr_2O_7$ (hypothetical pyrochlore phase) were calculated by the Vienna *ab initio* simulation package (VASP) [25,26] on the basis of density-functional theory (DFT). DFT calculations were performed using the projector-augmented wave (PAW) method [27]. Generalized gradient approximation (GGA) was employed as a electronic exchange-correlation potential. The plane wave cutoff energy was set as 450 eV. A 5 × 5 × 5 Monckhorst–Pack *k*-mesh was used for a primitive cell (22 atoms) to fully optimize the lattice constants and atomic positions. The convergence criteria were set as follows: 10^{-9} eV for total energy and 10^{-6} eV/Å for Hellmann–Feynman force. Real space force constants were calculated by the finite displacement method using a 2 × 2 × 2 supercell (176 atoms). The real space force constants for $(Nd_{0.5}Dy_{0.5})_2Zr_2O_7$ were estimated from the results obtained for $Nd_2Zr_2O_7$ and $Dy_2Zr_2O_7$ via the virtual crystal approximation (VCA) method, which has been proved to be applicable in a doped pyrochlore system [28]. Phonon properties were obtained from the calculated real space force constants by the PHONOPY software [29]. A 20 × 20 × 20 *q*-grid was applied in the phonon calculations. The Grüneisen parameter (γ) was calculated through a quasi-harmonic approximation (QHA) process. The cell volume was varied by ±1% with respect to equilibrium volume.

3 Results

3.1 Structure characterization

XRD and Raman spectra were used to characterize the $(Nd_{1-x}Dy_x)_2Zr_2O_7$ structure. When r_A/r_B is in the range of 1.46–1.78, $A_2B_2O_7$ forms an ordered pyrochlore structure (Fig. 1(a)). In the case of r_A/r_B < 1.46, $A_2B_2O_7$ crystallizes as a disordered fluorite (F) phase (Fig. 1(b)) [30]. For $RE_2Zr_2O_7$ with pyrochlore phases, cations and anions are not in a equivalent position, and the general formula can be more appropriately written as $A_2B_2O_6O'$. Under ideal circumstances, RE^{3+} and Zr^{4+} cations are located at the A and B sites (Wyckoff positions: 16*d* (1/2, 1/2, 1/2) and 16*c* (0, 0, 0)), respectively. O'^{2-} lies in the 8*b* Wyckoff position (3/8, 3/8, 3,8) with four RE^{3+} coordinated. Six O^{2-} anions are located in the 48*f* Wyckoff position (ε, 1/8, 1/8), surrounded by two RE^{3+} and two Zr^{4+}. Therefore, there is a free ε-parameter related to the r_A/r_B for 48*f* oxygen. There is an unoccupied site 8*a* (1/8, 1/8, 1/8) forming ordered oxygen vacancies. In fluorite-phase $RE_2Zr_2O_7$, all cation sites are equivalent and randomly occupied by RE^{3+} or Zr^{4+}. There is only one oxygen site in fluorite $RE_2Zr_2O_7$, which is 1/8 vacant, so this structure can be described as "defective fluorite", and the oxygen vacancies inside are completely disordered.

XRD results are shown in Fig. 2(a) with the primary peaks indexed. Phase compositions of the 11 samples can be divided into three groups: From x = 0 to x = 0.5, clear pyrochlore characteristic peaks exist; for example, a (331) peak at 2θ = 37° and a (511) peak at 2θ = 45°, so they can be assigned to the pyrochlore phase. From x = 0.7 to x = 1 (pure $Dy_2Zr_2O_7$), pure fluorite phases exist with no other superlattice peaks. The sample of x = 0.6 contains both pyrochlore and fluorite phases with similar lattice parameters, which means that there is a solubility limit in this binary system, as shown in a magnified XRD pattern in Fig. S1 in the Electronic Supplementary Material (ESM). The overall result reveals a transition process from an ordered pyrochlore structure to a disordered fluorite structure. With the increasing Dy content, the average ionic radius at the A site decreases, gradually approaching the Zr^{4+} radius at

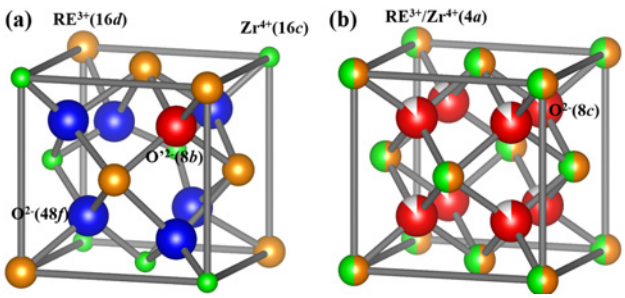

Fig. 1 Crystal structures of (a) 1/8 pyrochlore unit cell and (b) defect fluorite unit cell. Occupancy (Occ.) of anion site is 0.875.

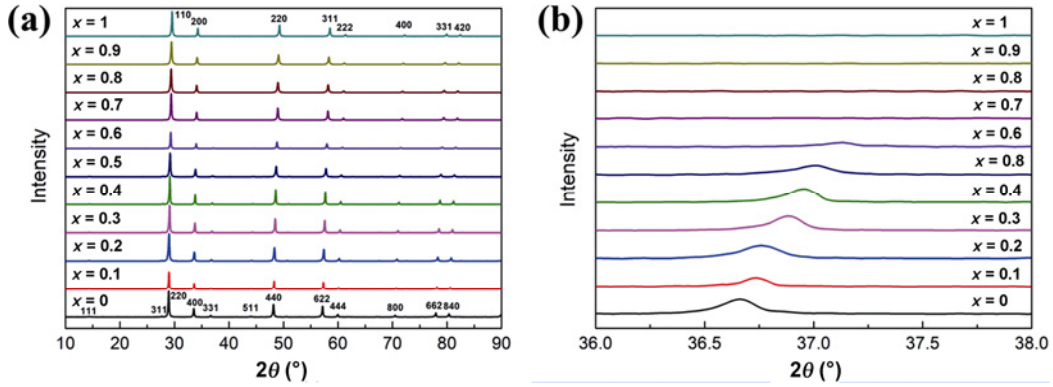

Fig. 2 (a) XRD patterns of $(Nd_{1-x}Dy_x)_2Zr_2O_7$ with x ranging from 0 to 1; (b) variations of pyrochlore (331) peaks.

the B site. As shown in Fig. 2(b), the (331) pyrochlore characteristic peak disappears at $x = 0.7$, indicating that the order–disorder transition occurs here. The r_A/r_B is 1.46 at this composition, which is in agreement with Refs. [30,31] on the phase transition critical point.

To deeply understand the order–disorder transition process, we carried out Rietveld refinement for all the single-phase samples. The refined lattice parameters are plotted in Fig. 3, where the lattice parameters of the fluorite compositions are doubled to be compared with those of pyrochlore compositions. Good linearity appears between x and the lattice parameter. Rietveld refinement graphs for $x = 0$, $x = 0.5$, and $x = 1$ are shown in Figs. 4(a)–4(c), with flat difference curves indicating good refinement quality. All the results are listed in Table 1, classified as pyrochlore and fluorite. Among the fluorite compositions, the structures are totally disordered. The Occ. of oxygen is 0.875, and $Nd^{3+}/Dy^{3+}/Zr^{4+}$ cations are distributed randomly at the 4*a* site. Among the pyrochlore compositions, the ε-parameter significantly increases with the increasing Dy content. This can be explained by the smaller radius of the Dy^{3+} ion (1.03 Å) compared with that of the Nd^{3+} ion (1.11 Å) [32]. The occurrence of Dy^{3+} at the A site reduces the average ionic radius, and then the 48*f* oxygen moves towards the A site; thus, the distance between the 48*f* oxygen and the B site is larger, which is proportional to the ε-parameter. The Occ. at the 8*a* site is no longer zero, and it also shows an increasing trend with x. This result indicates that the distribution of the oxygen vacancies is gradually disordered with a decrease in r_A/r_B. More oxygen vacancies appear at the 48*f* site but not at the 8*a* site. When r_A/r_B continues to

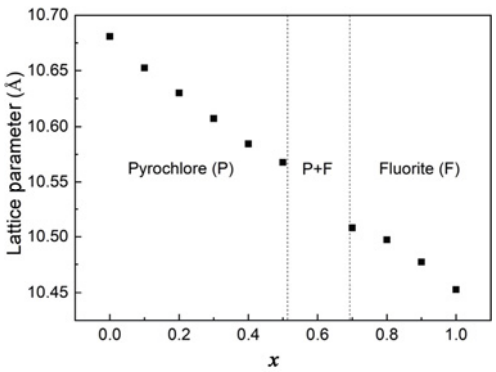

Fig. 3 Lattice parameters of single-phase $(Nd_{1-x}Dy_x)_2Zr_2O_7$ obtained by XRD Rietveld refinement. The data of fluorite phase compositions were doubled for comparison with those of pyrochlore.

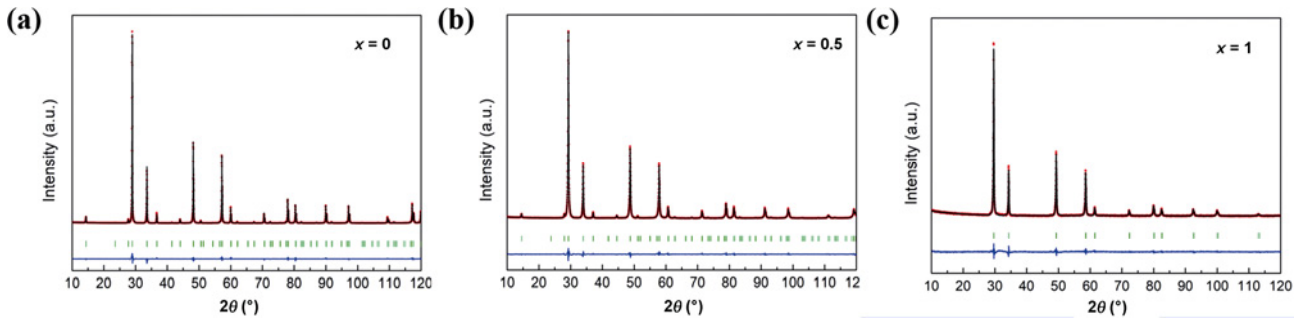

Fig. 4 Rietveld refinement graphs of (a) $Nd_2Zr_2O_7$, (b) $NdDyZr_2O_7$, and (c) $Dy_2Zr_2O_7$. Experimental and calculation results are shown in the red points and black lines, respectively; the difference curves between experiment and calculation are shown in the blue lines; and the green markers represent Bragg positions.

Table 1 Detailed Rietveld refinement results of single-phase $(Nd_{1-x}Dy_x)_2Zr_2O_7$: (a) pyrochlore compositions; (b) fluorite compositions

(a) Pyrochlore compositions

x	0	0.1	0.2	0.3	0.4	0.5
48*f* O ε-parameter	0.3312(4)	0.3322(8)	0.3361(6)	0.3360(6)	0.3377(6)	0.3402(6)
Zr 16*d* site Occ.	0.026(3)	0.092(1)	0.099(1)	0.062(1)	0.067(1)	0.126(1)
O 48*f* site Occ.	0.966(3)	0.943(6)	0.934(5)	0.905(4)	0.903(4)	0.913(5)
O 8*a* site Occ.	0.20(2)	0.34(4)	0.40(3)	0.57(3)	0.58(2)	0.52(3)
16*d* site B_{iso} (Å^2)	0.42(2)	0.24(3)	0.47(2)	0.68(2)	0.60(2)	0.51(2)
16*c* site B_{iso} (Å^2)	0.54(3)	1.25(5)	1.61(4)	1.69(4)	1.63(4)	1.72(4)
48*f* site B_{iso} (Å^2)	0.2(1)	1.3(2)	1.3(2)	1.9(2)	2.2(2)	2.4(2)
R_{wp} (%)	7.87	10.8	9.32	9.19	9.02	6.85
R_p (%)	5.68	7.78	6.89	6.81	6.75	5.05
R_{exp} (%)	4.24	4.45	4.18	4.22	4.21	4.47

(b) Fluorite compositions

x	0.7	0.8	0.9	1
4*a* site B_{iso} (Å^2)	1.53(2)	1.51(3)	1.55(3)	1.45(3)
8*c* site B_{iso} (Å^2)	3.7(1)	3.4(1)	3.3(1)	3.2(1)
R_{wp} (%)	4.19	4.23	4.08	4.25
R_p (%)	3.25	3.28	3.15	3.31
R_{exp} (%)	3.09	3.11	3.06	2.94

Note: B_{iso} (= $8\pi^2u^2$, where u^2 is the mean square displacement of the atom) is the isotropic atomic displacement parameter. R_{wp}, R_p, and R_{exp} are the quality factors of the refinement: $R_{wp} = \left\{\sum[w_i(Y_i^{exp} - Y_i^{calc})]^2 \Big/ \sum(w_iY_i^{exp})^2\right\}^{1/2}$, $R_p = \sum|Y_i^{exp} - Y_i^{calc}| \Big/ \sum Y_i^{exp}$, and $R_{exp} = \left[(n-P) \Big/ \sum(w_iY_i^{exp})^2\right]^{1/2}$. $w_i = (Y_i^{exp})^{-1/2}$, Y_i^{exp} is the experimental value, Y_i^{calc} is the calculated value, n is the number of data points, the sum is taken from i = 1 to n, and P is the number of refinement parameters. Numbers in parentheses correspond to the standard deviation of the last decimal place.

decrease, it results in the equivalence of all the oxygen sites and an eventual transition to a disordered fluorite phase. We use Zr Occ. at the A site (16*d*) to describe a cation antisite, and with the increasing x values, there is an upward trend with slight fluctuations. Zr Occ. at the A site in $(Nd_{0.5}Dy_{0.5})_2Zr_2O_7$ rises to 0.126 compared with that in the pure component $Nd_2Zr_2O_7$ (0.026), suggesting gradual homogenization between the 16*c* and 16*d* cation sites. Based on the analysis above, we can briefly conclude that the pyrochlore–fluorite transition is a gradual process involving oxygen vacancy disorder, cation homogenization, and positional movement of the 48*f* oxygen. The final status after the transition critical point is the complete random distribution of the cations at the 4*a* site and the oxygen anions or vacancies at the 8*c* site of fluorite.

Compared with the XRD, Raman spectroscopy is more sensitive to the local disorder in the anionic sublattice [33]. Raman spectroscopy is sensitive to oxygen–cation vibrations. In pyrochlore and fluorite, the ordering degree of the A and B cations and oxygen anions differs essentially, so it is easy to distinguish between the two by Raman spectroscopy. According to Ref. [34], there are six Raman active modes in pyrochlore, e.g., $\Gamma = A_{1g} + E_g + 4T_{2g}$. These modes involve the movement of the 48*f* oxygen and 8*b* oxygen. For an ideal fluorite structure, details in Raman spectra are lost due to the loss of translational symmetry induced by the randomly distributed oxygen vacancies, with one T_{2g} mode left behind. We plot Raman spectra for the $(Nd_{1-x}Dy_x)_2Zr_2O_7$ series, as shown in Fig. 5(a). Among the pyrochlore compositions, four of six Raman active modes can be clearly observed. These are the E_g mode at ~305 cm^{-1} related to O–RE–O bending vibration, the A_{1g} mode at ~505 cm^{-1} related to RE–O stretching, and two T_{2g} modes at ~400 and ~580 cm^{-1} representing Zr–O stretching and RE–O' stretching, respectively [35]. The broadness of these peaks is an excellent probe of the degree of the local disorder. When x gradually increases, obvious broadening occurs in all peaks. For the in-depth analysis, Raman peaks for all compositions are fitted, and then the full

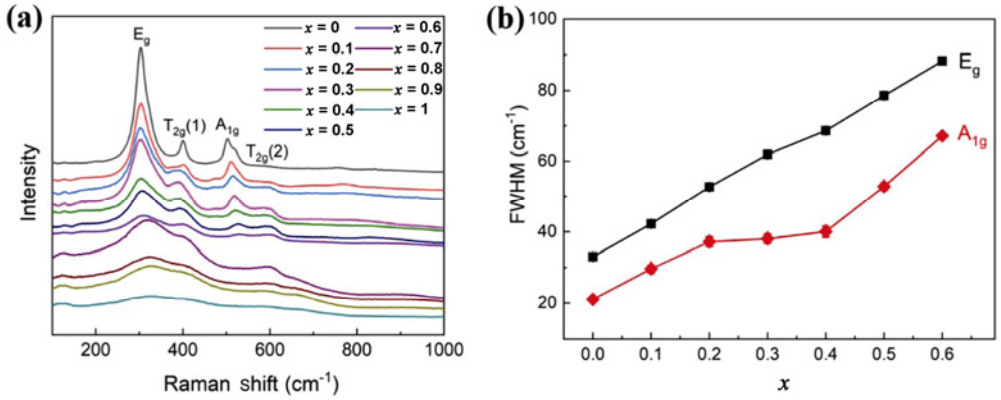

Fig. 5 (a) Raman spectra of $(Nd_{1-x}Dy_x)_2Zr_2O_7$; (b) FWHM of two intense peaks E_g and A_{1g} with x = 0–0.6.

width at half maximum (FWHM) for the two intense vibration modes E_g and A_{1g} for the compositions with $x < 0.7$ are plotted in Fig. 5(b). The FWHM values increase remarkably with higher x, which originates from the increasing disorder in the lattice. As shown in Rietveld refinement, cation antisites occur between the 16*c* and 16*d* sites, combined with the more random distribution of the oxygen vacancies. The periodicity is broken down to some degree, thereby relaxing the $k = 0$ selection rule [33,35] where k is the wave vector of phonon, which means that only phonons at Brillouin zone center contribute to Raman scattering. In a more disordered structure, some non-zone-center phonons also contribute to Raman scattering, producing broader Raman modes [35]. Another interesting phenomenon is that the intensity of the A_{1g} mode becomes lower with a higher x value. Then, the A_{1g} mode disappears at x = 0.7, which is the critical point composition where the order–disorder transition occurs. Zhou *et al.* [36] demonstrated that the A_{1g} mode is associated with only ε, and only A_{1g} mode significantly changes in intensity with changes in the polarization direction. The A_{1g} mode gradually decreases, which reflects the fact that the oxygen ion becomes disordered. Meanwhile, the frequency of the pyrochlore A_{1g} mode undergoes a blueshift with the increasing x, indicating a larger force constant for RE–O, which is consistent with Rietveld refinement. Raman spectroscopy results and analyses of the FWHM and A_{1g} mode intensity further demonstrate that the order–disorder transition occurs at x = 0.7, while it remains a gradual process even in the pyrochlore compositions.

3. 2 Thermal expansion properties

The thermal expansion rates (dL/L_0) from 40 to 1400 ℃ for all samples are shown in Fig. 6(a). Among the pyrochlore compositions, the significant thermal expansion improvement is observed over the whole temperature range when Dy is doped into the $Nd_2Zr_2O_7$ lattice. With the increasing Dy content, dL/L_0 increases, and then reaches a maximum value at x = 0.5. In contrast, the four fluorite compositions show very similar thermal expansion behaviors, which reflects their identical crystal structures. The thermal expansion drop occurs at the two-phase composition (x = 0.6), and the fluorite phase pulls down its thermal expansion property. The TEC values for the whole series at elevated temperatures of 1200, 1300, and 1400 ℃ are displayed in Fig. 6(b). The black dashed line connects the pure components at both ends and shows the TEC values following Vegard's law. A remarkable upward deviation from Vegard's law appears. The TEC values for pure $Nd_2Zr_2O_7$ and $Dy_2Zr_2O_7$ at 1400 ℃ are 9.90×10^{-6} and 11.02×10^{-6} K^{-1}, respectively, and then the assumed TEC value for x = 0.5 is calculated from Vegard's law to be 10.46×10^{-6} K^{-1}. Actually, the measured TEC value for x = 0.5 at 1400 ℃ is 11.36×10^{-6} K^{-1}, showing an enhancement of nearly 10% compared with the value calculated by Vegard's law. With the increasing Dy content, the degree of the TEC enhancement compared with the value predicted by Vegard's law increases in a pure pyrochlore region. When approaching the order–disorder transition, the degree of enhancement decreases until the TEC values gradually approach the line for Vegard's law in a fluorite region. The underlying mechanism for the pronounced TEC improvement in binary pyrochlore will be analyzed later, and the thermal expansion behavior of fluorite compositions will be discussed in Section 2 in the ESM.

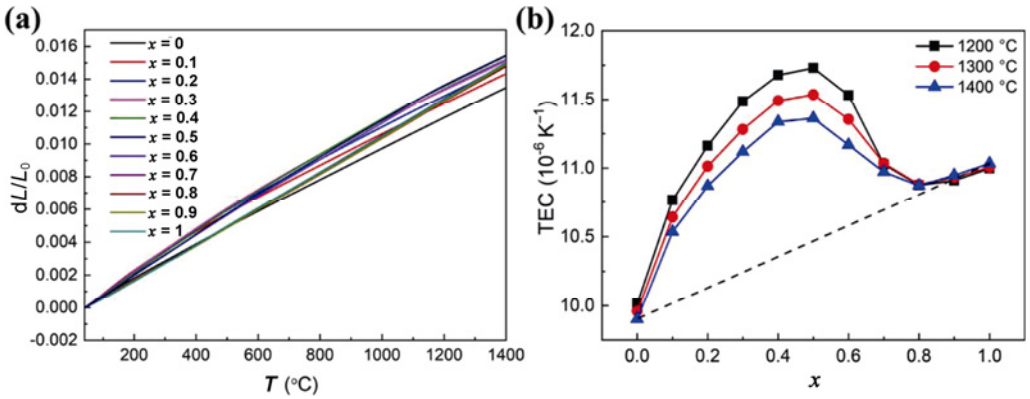

Fig. 6 (a) dL/L_0 for $(Nd_{1-x}Dy_x)_2Zr_2O_7$ from 40 to 1400 ℃; (b) TECs for $(Nd_{1-x}Dy_x)_2Zr_2O_7$ at 1200, 1300, and 1400 ℃. The black dashed line shows TEC value following Vegard's law.

4 Discussion

4. 1 Lattice energy variation

For $RE_2Zr_2O_7$, especially pyrochlore materials, the thermal expansion variation has traditionally been discussed from the viewpoint of the lattice energy [14,37]. The thermal expansion of solid materials is directly determined by the potential function curve, in which the cohesive energy ($U(R)$) of a crystal contains two parts: Madelung energy arising from Coulomb electrostatic attraction, following the R^{-1} rule, and the exchange interaction energy, which decreases rapidly as R (the interionic distance) increases. The two parts combine together, forming an asymmetrical curve, and $U(R)$ can be described with Born–Mayer potential [38].

$$U(R) = N(-Aq_Cq_A/R + z\lambda e^{-R/\rho}) \quad (4)$$

In this equation, N is the ion pair number, q_C and q_A are the charge numbers for the cations and the anions, respectively, z is the nearest atomic number, and λ and ρ are the empirical constants. The $U(R)$ reaches a minimum at the equilibrium position R_0, and when the temperature rises, R will fluctuate around R_0. In this anharmonic vibration, the distance of the ion vibration outwards is larger than that inwards, and statistically, the thermal expansion behavior appears. It is clear that Madelung energy affects the total $U(R)$ based on the equation for Born–Mayer potential. After Rietveld refinement, we confirmed an increase in the ε-parameter for the 48*f* oxygen during the disordering in pyrochlore. Based on the Rietveld refinement results, we calculated Madelung energy for the compositions with a single phase by MADEL in visualization for electronic and structural analysis (VESTA) [39]. The results are shown in Fig. 7(a), which are displayed as the electrostatic energy per asymmetric unit (E). To compare with those for pyrochlore, the values for the fluorite are multiplied by eight. Among the pure pyrochlore compositions, the electrostatic energy shows a smaller absolute value with the increasing ε-parameter, which is consistent with Refs. [40,41], indicating the softening of the lattice. When more Dy^{3+} cations with smaller radii replace Nd^{3+}, and more Zr^{4+} antisites appear, the average ionic radius of the A site decreases, and the 48*f* oxygen is pulled away from the B site with elongation and softening of the B–48*f* O bond. Actually, the strongest BO_6 octahedron maintains the pyrochlore frame [42]. Pannetier [41] calculated Madelung energy of the $A_2^{3+}B_2^{4+}O_6O'$ pyrochlore with a structure combining corner-sharing B_2O_6 units and zigzag A_2O' chains, and the interaction energy between B_2O_6 and A_2O' was also taken into consideration. Madelung energy decreased with a larger ε-parameter, and the B_2O_6 units had the most important influence among the three parts. Reference [41] proves again that the surrounding environment of the B site directly affects the thermal expansion properties. In other words, the weakening of the B–O bond leads to a higher TEC value. Among the pure fluorite compositions, the absolute values of electrostatic energy are lower than those of pyrochlore, but the TEC values decrease compared with that of x = 0.5. Therefore, there should be a mechanism beyond the lattice energy variation, which provides extra TEC improvement in pyrochlore, but does not work in fluorite.

As mentioned before, in many substitutional $RE_2Zr_2O_7$, the TEC values follow Vegard's law without the abnormal upward deviation found in our experiment,

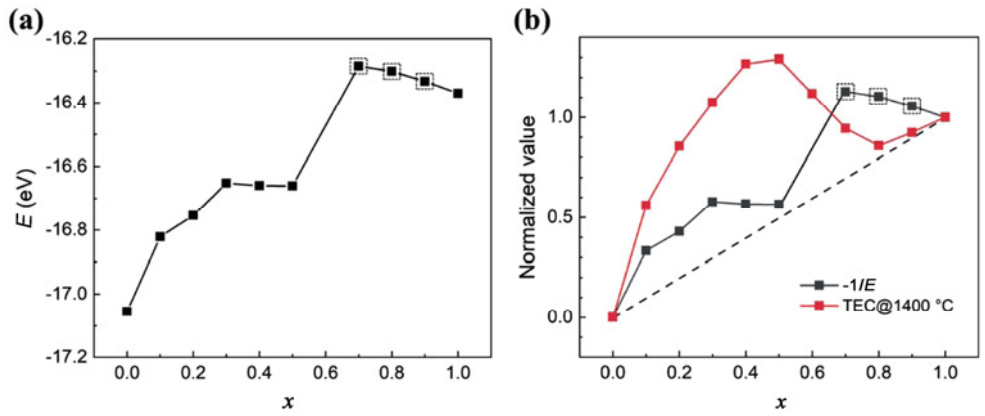

Fig. 7 (a) E of single-phase compositions; (b) comparison between normalized values of $-1/E$ and TEC at 1400 ℃ (the black dashed line shows Vegard's law). The black dashed squares mean uncertainty of data because possible ordering is ignored in Rietveld refinement of binary fluorite.

while the decreasing lattice energy with the increasing ε-parameter is also valid in these systems. Therefore, it is necessary to estimate how much contribution the lattice energy changes make to the improvement in the TEC values in our system. A semiempirical method was established by Zhang *et al*. [43] for the evaluation of the linear expansion coefficient (α) from the lattice energy. They used a new parameter that is proportional to the reciprocal of the lattice energy to form a linear relationship with α. We further simplify this model using $-1/E$ to compare with the TEC values. As shown in Fig. 7(b), the $-1/E$ and TEC values at 1400 ℃ are plotted together after normalization based on the values at x = 0 and 1. In the pyrochlore area, although the lattice energy curve is above Vegard's law line, it cannot fully contribute to such a large improvement in the TEC. Meanwhile, a higher difference appears with the larger Dy content among the pyrochlore compositions. Therefore, new factors should be taken into account for the additional TEC improvement of Dy-doped pyrochlore. We ascribe it to the fact that the Dy^{3+} doping results in stronger avoided crossing and higher anharmonicity, which is discussed based on our first-principles calculations in Section 4.2. Among the fluorite compositions, it appears that the TEC is suppressed. The order–disorder transition is a gradual process, and some ordering can appear in the fluorite lattice, which cannot be considered in our Rietveld refinement. In Raman spectra for the fluorite, the pyrochlore E_g mode does not completely disappear. The actual absolute value of the electrostatic energy with some ordering could be higher than that for a totally disordered structure. This means that the $-1/E$ value may be overestimated in fluorite. The rapid decrease of the TEC is due to the lack of avoided crossing because the cations are completely mixed in fluorite, and the localized vibration of RE^{3+}, which causes the avoided crossing, disappears, and then the anharmonicity will be much lower than that of pyrochlore. The lower lattice distortion degree is also a minor factor for the TEC decrease in fluorite.

4. 2 Effect of low-lying optical phonons on abnormal TEC

By first-principles calculations, we confirm that in the binary system, the Dy substitution leads to a lower frequency for the RE localized vibrational modes, and hence more avoided crossings and larger anharmonicity, which further enhance the thermal expansion property in addition to the effect of the lattice energy reduction. The phonon properties of $Nd_2Zr_2O_7$ and $(Nd_{0.5}Dy_{0.5})_2Zr_2O_7$ were calculated from the first-principles calculations for the further investigation of the TEC. Figure 8 shows the phonon band dispersions for $Nd_2Zr_2O_7$ and $(Nd_{0.5}Dy_{0.5})_2Zr_2O_7$. Band structures for $Nd_2Zr_2O_7$ and $(Nd_{0.5}Dy_{0.5})_2Zr_2O_7$ are quite similar at a high frequency. However, the band dispersions for the low-lying optical branches and acoustic branches become stronger when Dy is introduced into half of the Nd sites. This leads to a reduction of the frequency for the low-lying optical branches and a promotion of the transverse acoustic (TA)/TA' branches. As a result, the low-lying optical branches overlap with the TA/TA' branches not only at ~1 THz but also at ~2 THz, leading to mixing branches for $(Nd_{0.5}Dy_{0.5})_2Zr_2O_7$. As shown in Fig. 8, the TA/TA' branches for $Nd_2Zr_2O_7$

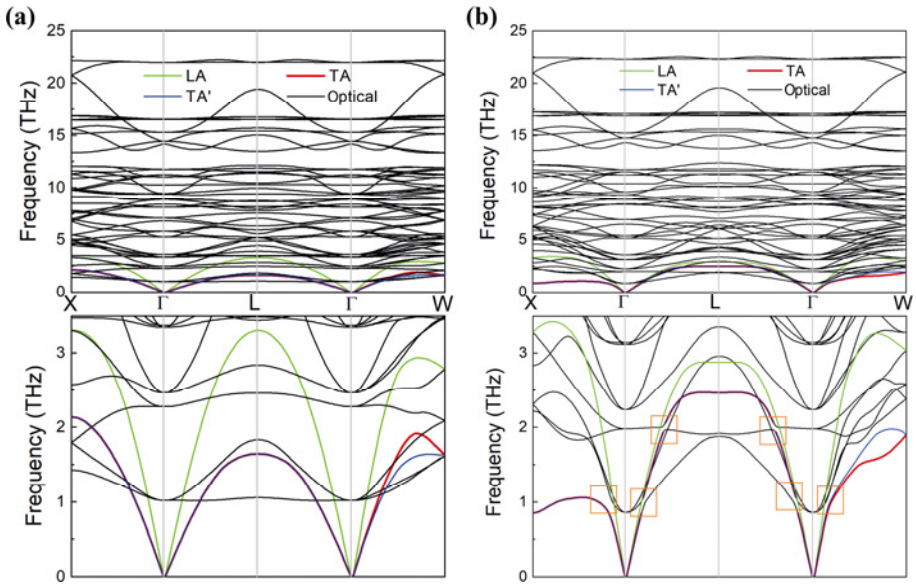

Fig. 8 Phonon band dispersions for (a) $Nd_2Zr_2O_7$ and (b) $(Nd_{0.5}Dy_{0.5})_2Zr_2O_7$. The squares mark areas of avoided crossings.

retain a linear character, while avoided crossings arise between the low-lying optical branches and the TA/TA' branches for $(Nd_{0.5}Dy_{0.5})_2Zr_2O_7$.

The partial density of states (PDOSs) for $Nd_2Zr_2O_7$ and $(Nd_{0.5}Dy_{0.5})_2Zr_2O_7$ were calculated for further investigation of the avoided crossings. As shown in Fig. 9, the low-lying optical phonon branches are primarily attributed to the vibration of RE^{3+} cations. According to Ref. [44], these localized phonon modes are so-called "rattling" modes, in which RE^{3+} is weakly bonded with surrounding atoms and exhibits the dominant vibrational amplitude. The reduced frequency for these localized modes in binary pyrochlore $(Nd_{0.5}Dy_{0.5})_2Zr_2O_7$ is caused by heavier Dy^{3+}, which pulls up the average mass of the RE site. These softened low-lying optical phonon branches appear to have more contact with TA/TA' branches, resulting in more avoided crossings.

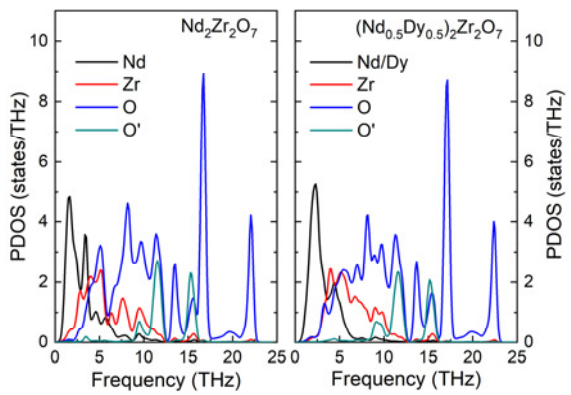

Fig. 9 PDOSs for $Nd_2Zr_2O_7$ and $(Nd_{0.5}Dy_{0.5})_2Zr_2O_7$.

The avoided crossings indicate strong anharmonicity and will result in violent changes in γ [45,46]. The average Grüneisen parameter (γ_{AV}) reflects the anharmonicity degree and is related to the volume thermal expansion coefficient (α_V) (Eq. (5)):

$$\alpha_V = \frac{\gamma_{AV} c_V}{V_m B} \tag{5}$$

where c_V is the molar specific heat at a constant volume defined as the sum of the contributions over all the modes, V_m is the molar volume, and B is the bulk modulus. The γ for $Nd_2Zr_2O_7$ and $(Nd_{0.5}Dy_{0.5})_2Zr_2O_7$ were calculated through the QHA process, and the results are shown in Fig. 10. The γ curves for the TA/TA' branches for $(Nd_{0.5}Dy_{0.5})_2Zr_2O_7$ show abrupt peaks at the same place where the avoided crossing

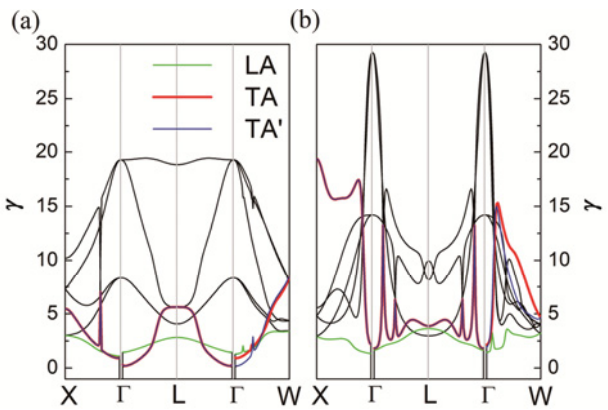

Fig. 10 γ corresponding to phonon states of (a) $Nd_2Zr_2O_7$ and (b) $(Nd_{0.5}Dy_{0.5})_2Zr_2O_7$. The black curves refer to low-lying optical branches.

appears. This can be ascribed to the mixing features of the low-lying branches of $(Nd_{0.5}Dy_{0.5})_2Zr_2O_7$ caused by heavier dopants at the RE site. The higher γ values indicate stronger anharmonicity for the vibrations in $(Nd_{0.5}Dy_{0.5})_2Zr_2O_7$, accordingly contributing to its thermal expansion. These results strongly support the above experiments for the thermal expansion properties of the $(Nd_{1-x}Dy_x)_2Zr_2O_7$ ceramics.

In recent years, researchers have paid more attention to the localized vibration of the RE in the RE pyrochlore. However, to the best of our knowledge, no direct relationship has been found between these modes and the thermal expansion of the RE pyrochlore. As competitive materials for TBC applications, the RE pyrochlore exhibits remarkably low thermal conductivity. Lan *et al*. [45] revealed the structural origin underlying their low thermal conductivity. In $Ln_2Zr_2O_7$ (Ln = La, Nd, Sm, and Gd), the first-principles calculations showed that TA/TA' acoustic branches overlap with the low-lying optical branches. The avoided crossing results in nonlinear acoustic dispersion curves away from the Γ point, leading to large γ for the TA/TA' branches. The TA/TA' branches are strongly scattered by the low-lying optical branches and contribute little to the thermal conductivity. The structural origin of these low-lying optical branches is found from the Ln vibration. In binary $RE_2Zr_2O_7$, $(La_{5/6}Yb_{1/6})_2Zr_2O_7$ was found to have very low glass-like thermal conductivity, and the heavy dopant Yb^{3+} gives rise to a "rattling" effect and promotes phonon scattering in the whole temperature range [47]. To further illustrate the enhanced voided crossing in binary pyrochlore, we carried out thermal conductivity measurements for x = 0 and 0.5. As shown in Fig. 11, x = 0.5 has lower thermal conductivity than x = 0, especially, it has a much lower value at room temperature.

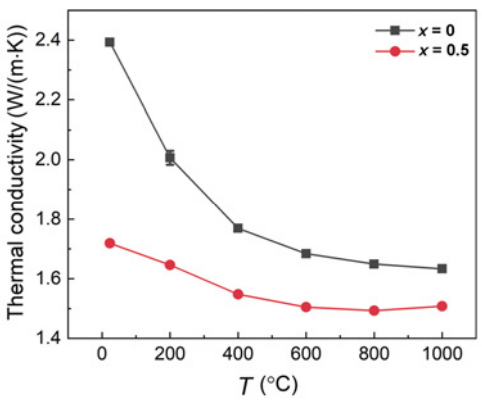

Fig. 11 Thermal conductivity for x = 0 and 0.5.

This sharp contrast indicates a higher level of acoustic phonon scattering in binary pyrochlore (x = 0.5), and its room-temperature thermal conductivity has already been shown to be suppressed. This result is consistent with our calculation, revealing higher anharmonicity at x = 0.5.

In consideration of high anharmonicity, the avoided crossing can be expected to have a great impact on the thermal expansion properties of the RE pyrochlore. However, in previous first-principles calculations, the predictions of the TEC values for $RE_2Zr_2O_7$ pyrochlore eliminated the localized modes [44]. Because lattice expansion softens these modes, and imaginary frequency appears, they only considered the stable phonon modes when calculating the TEC values. Our results reveal that the low-lying optical branches are softened by heavier dopants at the RE site and more overlap with the TA/TA' branches, leading to abruptly increasing γ. Therefore, the improved thermal expansion of binary zirconate pyrochlore is related to the localized vibration of RE atoms, providing a new mechanism for modifying the thermal expansion properties.

4. 3 Beyond Vegard's law

Previous studies on improving the thermal expansion of $RE_2Zr_2O_7$ barely mention the anharmonicity of the lattice. In our present research, the substitution of smaller and heavier RE ions can not only reduce $U(R)$ but also soften the low-lying optical phonons and cause the avoided crossing with more anharmonicity. Variation in $U(R)$ is common in substitutional $RE_2Zr_2O_7$ systems without an apparent avoided crossing effect; this may only lead to a TEC that fits Vegard's law but with no upward deviation. Based on our research and previous studies of the thermal expansion properties of the substitutional binary $RE_2Zr_2O_7$, we conclude that two conditions should be met to achieve TEC enhancement above Vegard's law: (i) Dopant ions should be heavy enough; (ii) the concentration of heavier RE ions in the pure pyrochlore region should be high enough. Obviously, fluorite is excluded. When both end compositions are fluorite phases, localized vibration modes disappear, and the lattice is not distorted either, such as $(Yb_xGd_{1-x})_2Zr_2O_7$ [16]. In some binary pyrochlore systems, the mass of the dopant may be too light to produce enough avoided crossing, and the TEC is still dominated by $U(R)$, such as $(Nd_{1-x}Gd_x)_2Zr_2O_7$ [15]. However, if both lanthanide

ions have too many differences in size, a wide two-phase region appears. In this region, considering the vanishing low-lying optical phonons and the low distortion level in the fluorite lattice, the effect of the avoided crossing is limited, and the TEC cannot be notably promoted, such as $(La_{1-x}Yb_x)_2Zr_2O_7$ [14]. In the pure pyrochlore region, the solubility of heavier RE ions is too low. In $(Nd_{1-x}Dy_x)_2Zr_2O_7$, the two-phase region is narrow, and at least half of the heavy Dy^{3+} can enter the RE site in pyrochlore. Sufficient solubility ensures apparently avoided crossing and promotes anharmonicity. Tuning the localized vibration of the RE can afford a new approach for improving the thermal expansion properties.

5 Conclusions

In this paper, we obtain high TECs exceeding the restriction of Vegard's law in $(Nd_{1-x}Dy_x)_2Zr_2O_7$. The transition from the ordered pyrochlore structure to the disordered fluorite structure occurs with the increasing x. The highest TEC value appears at x = 0.5, which contains the most Dy^{3+} dopant among the pure pyrochlore compositions. The decrease in the lattice energy cannot fully explain the upward deviation of the TEC from Vegard's law. Instead, the avoided crossing mechanism in pyrochlore aroused by the heavier Dy^{3+} doping is found to play a major role in the TEC improvement. The softened low-lying optical phonon branches, which correspond to the localized vibration of RE^{3+}, interact strongly with the acoustic phonon branches, fundamentally enhancing the anharmonicity. We believe that this finding can provide new opportunities for realizing smaller thermal mismatch and better stability during the high-temperature operation.

Acknowledgements

This work was supported by the National Natural Science Foundation of China (No. 52022042), the National Key R&D Program of China (No. 2021YFB3702300), and National Science and Technology Major Project (No. J2019-VII-0008-0148).

Declaration of competing interest

The authors have no competing interests to declare that are relevant to the content of this article.

Electronic Supplementary Material

Supplementary material is available in the online version of this article at https://doi.org/10.26599/JAC.2023.9220734.

References

[1] Lu TC, Yang J, Suo Z, *et al*. Matrix cracking in intermetallic composites caused by thermal expansion mismatch. *Acta Metall Mater* 1991, **39**: 1883–1890.

[2] Fitzpatrick ME, Hutchings MT, Withers PJ. Separation of macroscopic, elastic mismatch and thermal expansion misfit stresses in metal matrix composite quenched plates from neutron diffraction measurements. *Acta Mater* 1997, **45**: 4867–4876.

[3] Martena M, Botto D, Fino P, *et al*. Modelling of TBC system failure: Stress distribution as a function of TGO thickness and thermal expansion mismatch. *Eng Fail Anal* 2006, **13**: 409–426.

[4] Wei ZY, Meng GH, Chen L, *et al*. Progress in ceramic materials and structure design toward advanced thermal barrier coatings. *J Adv Ceram* 2022, **11**: 985–1068.

[5] Vaßen R, Jarligo MO, Steinke T, *et al*. Overview on advanced thermal barrier coatings. *Surf Coat Technol* 2010, **205**: 938–942.

[6] Cao XQ, Vassen R, Stoever D. Ceramic materials for thermal barrier coatings. *J Eur Ceram Soc* 2004, **24**: 1–10.

[7] Schlichting KW, Padture NP, Jordan EH, *et al*. Failure modes in plasma-sprayed thermal barrier coatings. *Mater Sci Eng* 2003, **342**: 120–130.

[8] Wu J, Wei XZ, Padture NP, *et al*. Low-thermal-conductivity rare-earth zirconates for potential thermal-barrier-coating applications. *J Am Ceram Soc* 2002, **85**: 3031–3035.

[9] Liu DB, Shi BL, Geng LY, *et al*. High-entropy rare-earth zirconate ceramics with low thermal conductivity for advanced thermal-barrier coatings. *J Adv Ceram* 2022, **11**: 961–973.

[10] Wang YH, Ma Z, Liu L, *et al*. Reaction products of $Sm_2Zr_2O_7$ with calcium–magnesium–aluminum–silicate (CMAS) and their evolution. *J Adv Ceram* 2021, **10**: 1389–1397.

[11] Feng J, Xiao B, Zhou R, *et al*. Thermal expansions of $Ln_2Zr_2O_7$ (Ln = La, Nd, Sm, and Gd) pyrochlore. *J Appl Phys* 2012, **111**: 103535.

[12] Zhu JT, Wei MY, Xu J, *et al*. Influence of order–disorder transition on the mechanical and thermophysical properties of $A_2B_2O_7$ high-entropy ceramics. *J Adv Ceram* 2022, **11**: 1222–1234.

[13] Lehmann H, Pitzer D, Pracht G, *et al*. Thermal conductivity and thermal expansion coefficients of the lanthanum rare-earth-element zirconate system. *J Am Ceram Soc* 2003, **86**: 1338–1344.

[14] Ren XR, Wan CL, Zhao M, *et al*. Mechanical and thermal

properties of fine-grained quasi-eutectoid $(La_{1-x}Yb_x)_2Zr_2O_7$ ceramics. *J Eur Ceram Soc* 2015, **35**: 3145–3154.

[15] Liu ZG, Ouyang JH, Zhou Y. Preparation and thermophysical properties of $(Nd_xGd_{1-x})_2Zr_2O_7$ ceramics. *J Mater Sci* 2008, **43**: 3596–3603.

[16] Liu ZG, Ouyang JH, Zhou Y, *et al*. Densification, structure, and thermophysical properties of ytterbium–gadolinium zirconate ceramics. *Int J Appl Ceram Technol* 2009, **6**: 485–491.

[17] Yang J, Zhao M, Zhang L, *et al*. Pronounced enhancement of thermal expansion coefficients of rare-earth zirconate by cerium doping. *Scripta Mater* 2018, **153**: 1–5.

[18] Wan CL, Qu ZX, Du AB, *et al*. Influence of B site substituent Ti on the structure and thermophysical properties of $A_2B_2O_7$-type pyrochlore $Gd_2Zr_2O_7$. *Acta Mater* 2009, **57**: 4782–4789.

[19] Qu ZX, Wan CL, Pan W. Thermal expansion and defect chemistry of MgO-doped $Sm_2Zr_2O_7$. *Chem Mater* 2007, **19**: 4913–4918.

[20] Guo L, Zhang Y, Wang CM, *et al*. Phase structure evolution and thermal expansion variation of Sc_2O_3 doped $Nd_2Zr_2O_7$ ceramics. *Mater Design* 2015, **82**: 114–118.

[21] Guo L, Li BW, Cheng YX, *et al*. Composition optimization, high-temperature stability, and thermal cycling performance of Sc-doped $Gd_2Zr_2O_7$ thermal barrier coatings: Theoretical and experimental studies. *J Adv Ceram* 2022, **11**: 454–469.

[22] Christensen M, Abrahamsen AB, Christensen NB, *et al*. Avoided crossing of rattler modes in thermoelectric materials. *Nat Mater* 2008, **7**: 811–815.

[23] Rodríguez-Carvajal J. FullProf. Available at https://cdifx.univ-rennes1.fr/fps/fp_rennes.pdf, 2000.

[24] Liang YJ, Che YC, Liu XX, *et al*. *Manual of Practical Inorganic Matter Thermodynamics*. Shenyang, China: Northeastern University Press, 1993. (in Chinese)

[25] Kresse G, Furthmüller J. Efficient iterative schemes for *ab initio* total-energy calculations using a plane-wave basis set. *Phys Rev B* 1996, **54**: 11169–11186.

[26] Kresse G, Hafner J. *Ab initio* molecular dynamics for liquid metals. *Phys Rev B* 1993, **47**: 558–561.

[27] Kresse G, Joubert D. From ultrasoft pseudopotentials to the projector augmented-wave method. *Phys Rev B* 1999, **59**: 1758–1775.

[28] Shu XY, Qing Q, Wen MF, *et al*. Experimentally and theoretically revealing the co-doping effects of Ce–Sr in $Gd_2Zr_2O_7$. *Langmuir* 2022, **38**: 11529–11538.

[29] Togo A, Tanaka I. First principles phonon calculations in materials science. *Scripta Mater* 2015, **108**: 1–5.

[30] Begg BD, Hess NJ, McCready DE, *et al*. Heavy-ion irradiation effects in $Gd_2(Ti_{2-x}Zr_x)O_7$ pyrochlores. *J Nucl Mater* 2001, **289**: 188–193.

[31] Sayed FN, Grover V, Bhattacharyya K, *et al*. $Sm_{2-x}Dy_xZr_2O_7$ pyrochlores: Probing order–disorder dynamics and multifunctionality. *Inorg Chem* 2011, **50**: 2354–2365.

[32] Shannon RD. Revised effective ionic radii and systematic studies of interatomic distances in halides and chalcogenides. *Acta Cryst* 1976, **32**: 751–767.

[33] Mandal BP, Banerji A, Sathe V, *et al*. Order–disorder transition in $Nd_{2-y}Gd_yZr_2O_7$ pyrochlore solid solution: An X-ray diffraction and Raman spectroscopic study. *J Solid State Chem* 2007, **180**: 2643–2648.

[34] Scheetz BE, White WB. Characterization of anion disorder in zirconate $A_2B_2O_7$ compounds by Raman spectroscopy. *J Am Ceram Soc* 1979, **62**: 468–470.

[35] Wan CL, Qu ZX, Du AB, *et al*. Order–disorder transition and unconventional thermal conductivities of the $(Sm_{1-x}Yb_x)_2Zr_2O_7$ series. *J Am Ceram Soc* 2011, **94**: 592–596.

[36] Zhou L, Huang ZY, Qi JQ, *et al*. Thermal-driven fluorite–pyrochlore–fluorite phase transitions of $Gd_2Zr_2O_7$ ceramics probed in large range of sintering temperature. *Metall Mater Trans A* 2016, **47**: 623–630.

[37] Guo L, Li MZ, Zhang Y, *et al*. Improved toughness and thermal expansion of non-stoichiometry $Gd_{2-x}Zr_{2+x}O_{7+x/2}$ ceramics for thermal barrier coating application. *J Mater Sci Technol* 2016, **32**: 28–33.

[38] Kittel C, McEuen P. *Introduction to Solid State Physics*, 7th edn. New York, USA: John Wiley & Sons, 1996.

[39] Momma K, Izumi F. VESTA: A three-dimensional visualization system for electronic and structural analysis. *J Appl Cryst* 2008, **41**: 653–658.

[40] Barker WW, White PS, Knop O. Pyrochlores. X. Madelung energies of pyrochlores and defect fluorites. *Can J Chem* 1976, **54**: 2316–2334.

[41] Pannetier J. Energie electrostatique des reseaux pyrochlore. *J Phys Chem Solids* 1973, **34**: 583–589. (in French)

[42] Hess NJ, Begg BD, Conradson SD, *et al*. Spectroscopic investigations of the structural phase transition in $Gd_2(Ti_{1-y}Zr_y)_2O_7$ pyrochlores. *J Phys Chem B* 2002, **106**: 4663–4677.

[43] Zhang SY, Li HL, Zhou SH, *et al*. Estimation thermal expansion coefficient from lattice energy for inorganic crystals. *Jpn J Appl Phys* 2006, **45**: 8801.

[44] Lan GQ, Ouyang B, Xu YS, *et al*. Predictions of thermal expansion coefficients of rare-earth zirconate pyrochlores: A quasi-harmonic approximation based on stable phonon modes. *J Appl Phys* 2016, **119**: 235103.

[45] Lan GQ, Ouyang B, Song J. The role of low-lying optical phonons in lattice thermal conductance of rare-earth pyrochlores: A first-principle study. *Acta Mater* 2015, **91**: 304–317.

[46] Tadano T, Gohda Y, Tsuneyuki S. Impact of rattlers on thermal conductivity of a thermoelectric clathrate: A first-principles study. *Phys Rev Lett* 2015, **114**: 095501.

[47] Wan CL, Zhang W, Wang YF, *et al*. Glass-like thermal conductivity in ytterbium-doped lanthanum zirconate pyrochlore. *Acta Mater* 2010, **58**: 6166–6172.